

# Electron ground state $g$ -factor in embedded InGaAs quantum dots: An atomistic study

Mustafa Kahraman<sup>1</sup> and Ceyhan Bulutay<sup>1,\*</sup>

<sup>1</sup>*Department of Physics, Bilkent University, Ankara 06800, Turkey*

(Dated: August 5, 2022)

We present atomistic computations within an empirical pseudopotential framework for the electron  $s$ -shell ground state  $g$ -tensor of embedded InGaAs quantum dots (QDs). A large structural set consisting of geometry, size, molar fraction and strain variations is worked out. The tensor components are observed to show insignificant discrepancies even for the highly anisotropic shapes. The family of  $g$ -factor curves associated with these parameter combinations coalesce to a single universal one when plotted as a function of the gap energy, thus confirming a recent assertion using a completely different electronic structure. Moreover, our work extends its validity to alloy QDs with various shapes and finite confinement that allows for penetration to the host matrix as in actual samples. Our set of results for practically relevant InGaAs QDs can help to accomplish through structural control,  $g$ -near-zero, or other targeted  $g$  values for spintronic or electron spin resonance-based direct quantum logic applications.

## I. INTRODUCTION

A single parameter, namely the  $g$ -factor, succinctly provides a measure of how strongly a charge in an electronic structure couples to an external magnetic field. Compared to its free-electron Dirac equation value of  $g_0 = 2$ , it can be significantly renormalized in solids, denoted by  $g^*$ , as a result of the spin-orbit interaction [1, 2]. Likewise, in semiconductor nanostructures such as quantum dots (QDs), yet another level of renormalization becomes operational by confining the carrier wave function around a heterogeneous region which accordingly tailors the orbital contribution [3], besides offering electrical tunability [4–8]. Among these structures, the self-assembled InGaAs QDs particularly stand out where a number of critical quantum technological milestones have been demonstrated, like indistinguishable single-photon sources [9], and on demand [10], spin-resolved resonance fluorescence [11], spin-photon interface [12], entangled photon pairs [13], entanglement swapping [14], as well as simultaneous antibunching and squeezing [15]. Interestingly, the electron spin resonance (ESR) in *embedded* InGaAs QDs has so far been elusive, with the exception of one group which awaits to be reproduced for more than a decade [16]. As a matter of fact, ESR would be highly welcomed in embedded QDs for the direct magnetic field control of the electron spin over the full Bloch sphere, which was unambiguously showcased much earlier in electrostatically defined gated QDs [17].

An intriguing region that also merits attention is where the QD  $g$ -factor changes sign, which is of relevance to  $g$ -near-zero QDs ( $g^* \sim 0$ ). There are a number of reasons why this can bring interesting physics. In general the background nuclear spins interact with external magnetic field with a coupling constant about three orders of magnitude smaller than those of free electrons, originating

from their Landé factor ratio [18]. Consequently, nuclear magnetic resonance (NMR) and ESR frequencies are off by again a factor of thousand.  $g$ -near-zero QDs mitigate the ESR and NMR mismatch so that the electron-nucleus counter spin flips become energetically more affordable. This can be utilized to achieve a strong coupling between electron and the nuclear spin bath, similar to the Hartmann-Hahn double resonance [19–21]. From a basic science point of view,  $g$ -near-zero can promote spin-density wave state where the spins are oriented perpendicular to the magnetic field [22], and a spin texture of skyrmionic excitations [23]. As to some practical examples, it can facilitate controlled spin rotation by  $g^*$ -tunability provided that it changes sign via electric gating [4, 24], or the quantum state transfer between a flying photon qubit and a resident electron spin qubit in a QD [25]. Thus, a deeper understanding of the elements that govern the  $g$ -factor, especially in InGaAs QDs, is quite valuable for several research directions.

Over the years there has been a number of experimental efforts to better characterize the  $g$ -factor of InGaAs QDs [26–36]. A complication that arises in most of these magnetoluminescence-based measurements is the extraction from the *excitonic*  $g$ -factor that of the electronic contribution [6, 8, 27, 28, 31, 32, 34, 35], which hinders its sign, a concern also shared by the magnetocapacitance [29], and photocurrent spectroscopy experiments [36]. Naturally, they need to be supplemented by an electronic structure theory, which has been routinely a variant of the  $k \cdot p$  model [37–41], even though more sophisticated alternatives are being developed [42–45]. Another difficulty that virtually affects all experimental studies stems from not knowing the precise structural information such as the alloy composition, geometry and hence the strain profile of the *probed* single QD. Hitherto, what is available at best is a statistical data for the whole sample. Notwithstanding, according to some of these works, this lack of knowledge may not be so critical as it is primarily the gap energy that is directly linked with the  $g$ -factor

\* bulutay@fen.bilkent.edu.tr

[5, 31], thereby substantiating the celebrated so-called Roth-Lax-Zwerdling expression that was originally derived for bulk [46]. A recent tight-binding analysis qualitatively supported this by concluding that the dominant contribution to the  $g$ -factor of nanostructures comes from the bulk term, considering only the compound QDs [47]. Undoubtedly, these assertions merit further theoretical investigation, preferably by an atomistic electronic structure technique that can provide quantitative insights into *alloy* InGaAs QDs as it is predominantly for the so far studied ones [4, 6, 7, 26–28, 31, 32].

In this work, we consider  $\text{In}_x\text{Ga}_{1-x}\text{As}$  QDs embedded in a host matrix and under a homogeneous compressive hydrostatic strain which is typical for the inner cores of the relaxed structures [48–50]. The studied geometries range from full spherical down to a lens shape as well as various cuts in between with respect to [111] axis. Independently, the indium fraction is also varied giving rise to a uniform alloy profile inside the QD. These structures embody on the order of 10 million atoms including the matrix material which makes it imperative to use an efficient atomistic electronic structure tool. In our case we employ the so-called linear combination of bulk bands (LCBB) which handles such atomic numbers with reasonable computational budget [51]. In the past, we used it in nanocrystals for the linear optical response [52], third-order nonlinear optics [53], electroabsorption [54], and coherent population transfer [55], and in nanowire structures for electronic structure [56] and ballistic transport [57]. To the best of our knowledge this is the first application of the LCBB method to the study of  $g$ -factor in semiconductors.

Most importantly, among other findings, our work substantiates the conclusion of the aforementioned tight-binding study which reported a universal behavior for  $g^*$  when plotted with respect to the gap energy [47]. Furthermore, we extend its validity to alloy QDs of various shapes and finite confinement that allows for penetration to the matrix as in realistic samples.

The organization of the paper is as follows: in Section II we describe the LCBB technique as it is not widely known, and the  $g$ -factor expressions. Section III presents our results for a rich variety of QD structures, and reveal the underlying universal behavior followed by our conclusions in Section IV. Some computational details are spared for the Appendix.

## II. THEORY

### A. LCBB Electronic Structure Technique

A general necessity in atomistic electronic structure techniques is a large basis set, as in the form of extended plane waves or localized Gaussian orbitals, so as not to compromise accuracy, which inevitably inflates the computational budget. Yet, when a restricted energy window is of interest, a specialized basis set of modest size se-

lected with physical insight becomes viable, forming the premise of the LCBB method [51]. Here, the basis set is formed by the bulk Bloch functions of the underlying materials within the desired energy range. Hence, the  $j^{\text{th}}$  stationary state wave function of a nanostructure is approximated by the expansion

$$\psi_j(\mathbf{r}) = \frac{1}{\sqrt{N}} \sum_{n,\mathbf{k},\mu} C_{n\mathbf{k}}^{\mu,j} u_{n\mathbf{k}}^\mu(\mathbf{r}) e^{i\mathbf{k}\cdot\mathbf{r}}, \quad (1)$$

where  $N$  is the number of bulk primitive unit cells inside the large supercell of the nanostructure,  $n$  is the bulk band index,  $\mathbf{k}$  is the wave vector within the first Brillouin zone of the underlying lattice, and  $\mu$  designates the materials in the set, usually the core and the embedding media. In this expression the cell-periodic part  $u_{n\mathbf{k}}^\mu(\mathbf{r})$  of the bulk Bloch functions of each material has the Fourier series representation

$$u_{n\mathbf{k}}^\mu(\mathbf{r}) = \frac{1}{\sqrt{\Omega_0}} \sum_{\mathbf{G}} B_{n\mathbf{k}}^\mu(\mathbf{G}) e^{i\mathbf{G}\cdot\mathbf{r}},$$

where the summation is over the reciprocal lattice vectors  $\mathbf{G}$ , inside an energy cut-off, and  $\Omega_0$  is the volume of the primitive cell [2]. The Fourier coefficients  $B_{n\mathbf{k}}^\mu(\mathbf{G})$  are presumably available by diagonalizing the bulk Hamiltonian of material  $\mu$  at each  $\mathbf{k}$  point.

The single-particle Hamiltonian of a nanostructure constitutes the kinetic energy and the crystal potential parts. For the latter we employ the empirical pseudopotentials [58] to describe the atomistic environment

$$\begin{aligned} \mathcal{H} &= \mathcal{T} + \mathcal{V}_{\text{xtal}} \\ &= -\frac{\hbar^2 \nabla^2}{2m_0} + \sum_{\mu, \mathbf{R}_l, \alpha} W_\alpha^\mu(\mathbf{R}_l) v_\alpha^\mu(\mathbf{r} - \mathbf{R}_l - \mathbf{d}_\alpha^\mu), \end{aligned}$$

where  $m_0$  is the free electron mass, the direct lattice vector  $\mathbf{R}_l$  indicates the origin for the primitive cell, and  $\mathbf{d}_\alpha^\mu$  specifies the relative coordinate of the basis atom  $\alpha$  within the primitive cell. The weight function  $W_\alpha^\mu(\mathbf{R}_l)$  keeps the information about the atomistic composition of the nanostructure by taking values 0 or 1 depending on the type of the atom located at the position  $\mathbf{R}_l + \mathbf{d}_\alpha^\mu$ .  $v_\alpha^\mu$  is the local screened spherical atomic pseudopotential of atom  $\alpha$  of the material  $\mu$  [58].

Hamiltonian matrix elements are evaluated with respect to the LCBB basis states,  $\{|n\mathbf{k}\mu\rangle\}$  which can be cast into a generalized eigenvalue problem

$$\sum_{n,\mathbf{k},\mu} \langle n'\mathbf{k}'\mu' | \mathcal{T} + \mathcal{V}_{\text{xtal}} | n\mathbf{k}\mu \rangle C_{n\mathbf{k}}^{\mu,j} = E_j \sum_{n,\mathbf{k},\mu} C_{n\mathbf{k}}^{\mu,j} \langle n'\mathbf{k}'\mu' | n\mathbf{k}\mu \rangle,$$

which yields the energy  $E_j$  and the expansion coefficients  $C_{n\mathbf{k}}^{\mu,j}$ . The explicit forms of these matrix elements are

$$\langle n'\mathbf{k}'\mu' | n\mathbf{k}\mu \rangle = \delta_{\mathbf{k},\mathbf{k}'} \sum_{\mathbf{G}} [B_{n'\mathbf{k}'}^{\mu'}(\mathbf{G})]^* B_{n\mathbf{k}}^\mu(\mathbf{G}),$$

$$\langle n'\mathbf{k}'\mu' | \mathcal{T} | n\mathbf{k}\mu \rangle = \delta_{\mathbf{k},\mathbf{k}'} \sum_{\mathbf{G}} \frac{\hbar^2 |\mathbf{k} + \mathbf{G}|^2}{2m_0} [B_{n'\mathbf{k}'}^{\mu'}(\mathbf{G})]^* B_{n\mathbf{k}}^\mu(\mathbf{G}),$$

$$\begin{aligned} \langle n' \mathbf{k}' \mu' | \mathcal{V}_{\text{xtal}} | n \mathbf{k} \mu \rangle = & \sum_{\mathbf{G}, \mathbf{G}'} [B_{n' \mathbf{k}'}^{\mu'}(\mathbf{G}')]^* B_{n \mathbf{k}}^{\mu}(\mathbf{G}) \\ & \times \sum_{\mu'', \alpha} \mathcal{V}_{\alpha}^{\mu''}(|\mathbf{k} + \mathbf{G} - \mathbf{k}' - \mathbf{G}'|) \\ & \times \mathcal{W}_{\alpha}^{\mu''}(\mathbf{k} - \mathbf{k}') e^{-i(\mathbf{k} + \mathbf{G} - \mathbf{k}' - \mathbf{G}') \cdot \mathbf{d}_{\alpha}^{\mu''}}. \end{aligned}$$

Here,  $\mathcal{V}_{\alpha}^{\mu''}$  and  $\mathcal{W}_{\alpha}^{\mu''}$  are the Fourier transforms of atomic pseudopotentials and the weight functions

$$\begin{aligned} \mathcal{V}_{\alpha}^{\mu''}(|\mathbf{k} + \mathbf{G} - \mathbf{k}' - \mathbf{G}'|) &= \frac{1}{\Omega_0} \\ & \int v_{\alpha}^{\mu''}(\mathbf{r}) e^{i(\mathbf{k} + \mathbf{G} - \mathbf{k}' - \mathbf{G}') \cdot \mathbf{r}} d^3 r, \quad (2) \\ \mathcal{W}_{\alpha}^{\mu}(\mathbf{k} - \mathbf{k}') &= \sum_j W_{\alpha}^{\mu}(\mathbf{R}_j) e^{i(\mathbf{k} - \mathbf{k}') \cdot \mathbf{R}_j}. \quad (3) \end{aligned}$$

### B. Spin-orbit interaction

So far, only the spin independent part of the Hamiltonian is considered. Following Hybertsen and Louie [59], the spin-orbit interaction can be incorporated as

$$\mathcal{H}_{SO} = \sum_{\ell=1}^{\infty} |\ell\rangle V_{\ell}^{SO}(r) \ell \cdot \boldsymbol{\sigma} \langle \ell|, \quad (4)$$

where,  $\ell$  is the orbital angular momentum label,  $\boldsymbol{\sigma}$  is the Pauli spin matrix, and  $V_{\ell}^{SO}(r)$  is the angular-momentum-dependent (i.e., nonlocal) radial spin-orbit potential. To simplify, we restrict to the dominant  $\ell = 1$ , i.e.,  $p$  component, and the spin-orbit matrix elements become

$$\begin{aligned} \langle s, \mathbf{K} | \mathcal{H}_{SO} | s', \mathbf{K}' \rangle = & -i \langle s | \boldsymbol{\sigma} | s' \rangle \cdot \left[ 12\pi \frac{\mathbf{K} \times \mathbf{K}'}{KK'} V_{\ell=1}^{SO}(K, K') \right] \\ & \times S(\mathbf{K}' - \mathbf{K}), \quad (5) \end{aligned}$$

where  $\mathbf{K} = \mathbf{k} + \mathbf{G}$ ,  $\mathbf{K}' = \mathbf{k}' + \mathbf{G}'$ ,  $|s\rangle$  denotes a spinor state,  $S(\mathbf{K}' - \mathbf{K})$  is the bulk static structure factor.  $V_{\ell}^{SO}(K, K')$  is given by the integral

$$V_{\ell}^{SO}(K, K') = \int_0^{\infty} \frac{dr}{\Omega_0} r^2 j_{\ell}(Kr) V_{\ell}^{SO}(r) j_{\ell}(K'r), \quad (6)$$

with  $j_{\ell}$  being the spherical Bessel function of the first kind and  $V_{\ell}^{SO}(r)$  is chosen as a Gaussian function [60] with a width of 2.25 Bohr radius and its amplitude being a fit parameter as described below.  $V_{\ell}^{SO}(K, K')$  is computed once, and invoked from a look-up table.

### C. $g$ -factor

Unlike a free electron, the charge of a nanostructure experiences an anisotropic coupling to an external magnetic field  $\mathbf{B}$  so that its  $g$ -factor becomes a rank-2 symmetric tensor  $\vec{g}$ , which becomes diagonal when expressed in its principal axes; it is described through the Zeeman Hamiltonian

$$\mathcal{H}_Z = \frac{1}{2} \mu_B \boldsymbol{\sigma} \cdot \vec{g} \cdot \mathbf{B}, \quad (7)$$

where  $\mu_B$  is the Bohr magneton [37]. The celebrated  $\vec{g}$  expression follows from a spinless electronic structure calculation when the spin-orbit interaction is included as a first-order perturbation [2, 61]. This bulk formulation can be extended to QDs in terms of the matrix elements between two confined states  $n$  and  $j$  as

$$\mathbf{p}_{nj} = \frac{(2\pi)^3}{\Omega_{\text{SC}}} \int_{\text{SC}} \psi_n^*(\mathbf{r}) \mathbf{p} \psi_j(\mathbf{r}) d^3 r, \quad (8)$$

$$\mathbf{h}_{nj} = \frac{(2\pi)^3}{\Omega_{\text{SC}}} \int_{\text{SC}} \psi_n^*(\mathbf{r}) \mathbf{h} \psi_j(\mathbf{r}) d^3 r, \quad (9)$$

where the integrals are over the supercell volume  $\Omega_{\text{SC}}$ ,  $\mathbf{p}$  is the momentum operator, and  $\mathbf{h}$  is the spin-orbit related operator defined through  $\mathcal{H}_{SO} = \mathbf{h} \cdot \boldsymbol{\sigma}$ ; see, Eq. (4). This yields

$$\begin{aligned} \vec{g}_n = 2\vec{I} + \frac{2}{i\hbar^2 m_0} \sum_{jl} \frac{1}{\omega_{nj}} \left\{ \frac{(\mathbf{h}_{jl} - \mathbf{h}_{lj})(\mathbf{p}_{nj} \times \mathbf{p}_{ln})}{\omega_{jl}} \right. \\ \left. + \frac{(\mathbf{h}_{ln} - \mathbf{h}_{nl})(\mathbf{p}_{nj} \times \mathbf{p}_{jl})}{\omega_{nl}} \right\}, \quad (10) \end{aligned}$$

where  $\vec{I}$  is the  $3 \times 3$  identity matrix, and  $\omega_{nj} = (E_n - E_j)/\hbar$ , and etc. With some manipulations, it can be shown to be equivalent to the Roth's bulk expression [61]

$$\begin{aligned} \vec{g}_n = 2\vec{I} + \frac{2}{i\hbar^2 m_0} \sum_{jl}' \frac{1}{\omega_{nj} \omega_{nl}} \{ \mathbf{h}_{nj} \mathbf{p}_{jl} \times \mathbf{p}_{ln} \\ + \mathbf{h}_{jl} \mathbf{p}_{nj} \times \mathbf{p}_{ln} + \mathbf{h}_{ln} \mathbf{p}_{nj} \times \mathbf{p}_{jl} \}. \quad (11) \end{aligned}$$

but now the matrix elements are worked out using nanostructure states as given by Eqs. (8), (9).

## III. RESULTS

### A. Cuts from a sphere

We start with the compound InAs spherical QD of 45 nm diameter embedded in a host matrix, where the QD is under a 2% compressive strain, corresponding to a hydrostatic strain of  $\epsilon_H = -0.06$ . In Fig. 1 we see how  $\vec{g}$  varies along its principal directions when the sphere is successively cut by a (111) oriented plane, producing in addition to a sphere, a hydrophobic-contact-angle-, hemispherical-, and lens-shaped QDs. As expected, the increasing confinement gradually modifies  $g^*$  from -2.47 to 0.21 so that  $g^* \sim 0$  would be attained for a lens shaped QD with a bigger diameter than the one in Fig. 1. The three principal values of  $\vec{g}$  marginally deviate from each other even though they become exceedingly of anisotropic shapes toward the lens QD. The largest difference is about 0.03 that occurs for the spherical QD which indicates the numerical accuracy of our calculations. This lack of anisotropy in  $\vec{g}$  is ubiquitous for all the structures studied in this work. Therefore, for the

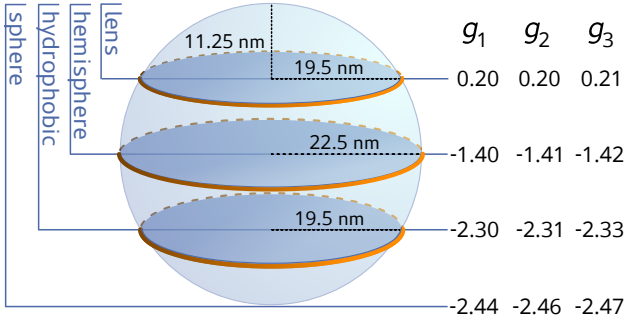


FIG. 1. The three principal  $\vec{g}$  values of embedded InAs QDs under 2% homogeneous compressive strain. The four geometries originate from a sphere by cutting with a (111) plane producing lens, hemisphere, and hydrophobic-contact-angle spherical domes.

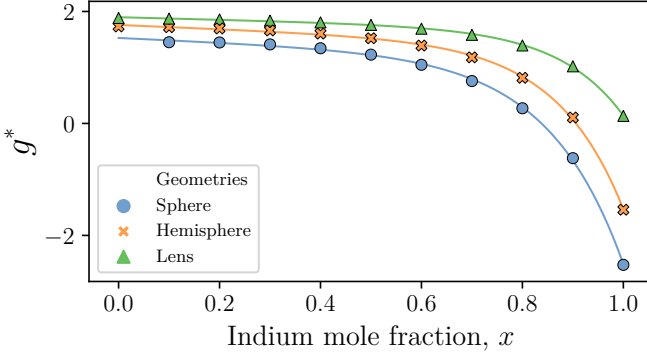


FIG. 2. Variation of the  $g$ -factor of the spherical-, hemispherical- and lens-shaped  $\text{In}_x\text{Ga}_{1-x}\text{As}$  QDs under  $-2\%$  homogeneous strain as a function of the indium mole fraction. All of them have the same diameter of 46 nm, and the lens QDs have a height about 11-12 nm. Lines are to guide the eye.

sake of clarity, we shall display its major principal component in the plots to follow.

Next, choosing the spherical, hemispherical, and lens geometries from Fig. 1, we consider how  $g$ -factor evolves with the indium mole fraction, for alloy  $\text{In}_x\text{Ga}_{1-x}\text{As}$  QDs with a diameter around 45 nm, and for the lens ones of height about 11-12 nm. Fig. 2 illustrates the family of curves belonging to each shape for the QD strain value of  $-2\%$ , i.e.,  $\epsilon_{xx} = \epsilon_{yy} = \epsilon_{zz} = -0.02$ . The geometric sensitivity only reveals itself toward the indium-rich composition, where the sign change in  $g^*$  also takes effect. Stated differently, indium-poor QDs offer very limited  $g$ -tunability.

### B. Dimensional dependence in lens QDs

In the remaining sections we concentrate on the more prevailing lens-shaped QDs. First, we present in Fig. 3 the set of curves for a wide range of indium mole frac-

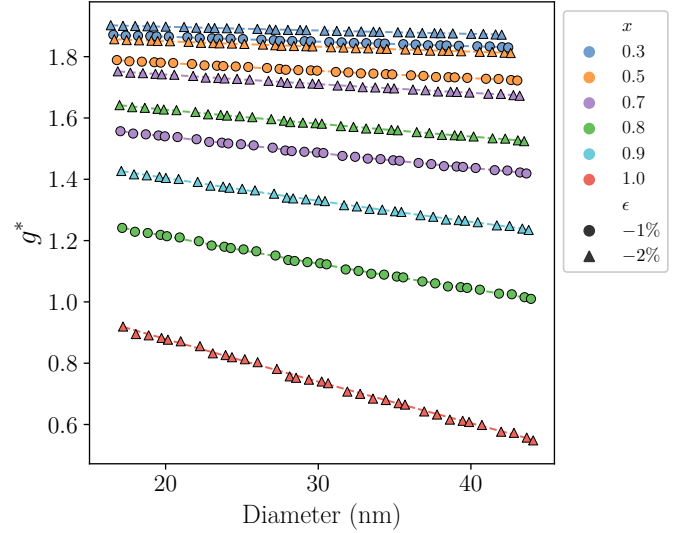


FIG. 3. Variation of  $g$ -factor with the diameter of the lens QD. The family of curves are all at a fixed aspect ratio of  $h/D = 0.2$  for different indium mole fraction, and strain values. Dashed lines are to guide the eye.

tions, and for two different strains, all at a fixed aspect ratio (height over diameter),  $h/D = 0.2$ . Most notably,  $g$ -factor is seen to raise with compressive strain. Among possible reasonings, it is the orbital momentum quenching through enhanced electron confinement under strain that is responsible here [35, 38]. To quote some typical values in our case, due to larger hydrostatic deformation potential of the conduction band edge of the matrix material with respect to  $\text{In}_x\text{Ga}_{1-x}\text{As}$ , for  $x = 0.3$  the conduction band offset between core and matrix materials increases from 269 meV to 366 meV as the core material strain changes from  $-1\%$  to  $-2\%$ . Like Fig. 2, the geometric  $g$ -factor variation under strain gets diminished with the decreasing molar fraction,  $x$ . Therefore, for low indium concentration and higher strain,  $g^*$  approaches to free-electron value and becomes largely QD size independent. As the indium content increases, so does the contribution of spin-orbit interaction that lowers  $g^*$  and instates its size dependence.

Another set of curves follows from, this time varying the QD height, keeping the lens basal diameter fixed at 35 nm as shown in Fig. 4. The general trends are similar to Fig. 3, but display a wider change under height, and in turn aspect ratio. For the considered lens diameter,  $g^* \sim 0$  ensues very close to InAs composition and for low strain values. An intriguing observation is that different mole fraction and strain curves can perfectly overlap as in ( $x = 0.5$ ,  $\epsilon = -0.01$ ) and ( $x = 0.8$ ,  $\epsilon = -0.03$ ), which indicates that, as far as  $g$ -factor is concerned, the effect of one can be undone with the other physical parameter. This suggests a universal dependence under a decisive parameter, as we discuss next.

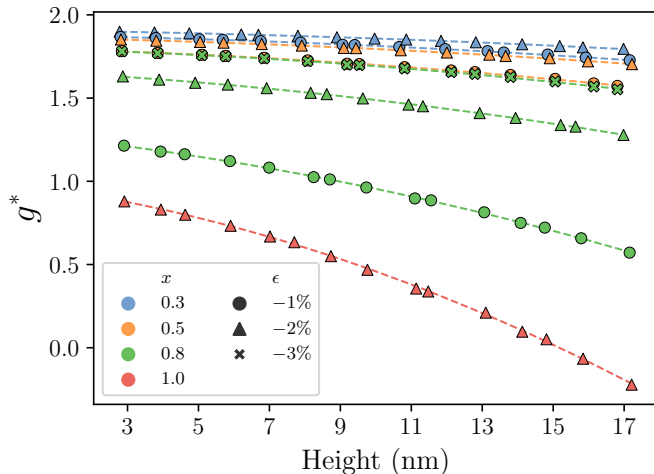


FIG. 4. Variation of  $g$ -factor with the height of the lens QD for a fixed basal diameter of 35 nm. The family of curves are for different indium mole fraction, and strain values. Dashed lines are to guide the eye.

### C. Universality with respect to gap energy

Finally, we now recast all the various QD  $g$ -factor results above as function of the single-particle gap energy,  $E_g$  that separates conduction and valence states for each case. If need be, it can be readily extended to include the excitonic binding energy [54], in connection to low-temperature magnetoluminescence experiments. When we replot the data in Figs. 2, 3 and 4 in this manner we observe that all the distinct family of curves for various mole fractions, strains, aspect ratios and heights coalesce to a universal curve as presented in Figs. 5 (a)-(c), respectively. This not only supports the earlier finding of Ref. [47], but also extends it to alloys while allowing for penetration into surrounding matrix material. All these data can be faithfully represented, especially from free-electron value to where  $g^*$  changes sign, by a curve of the form  $g^*(E_g) = 2 - (E_0/E_g)^2$  involving only a single fit parameter  $E_0 = 1.5665$ , making it even simpler than that of Ref. [47]. Two other data from the literature [27, 31] as shown in Fig. 5 (a), also fall close to this curve. In the pursuit of  $g$ -factor engineering, this universality warrants a recipe by merely tuning the gap energy through any means [28, 62].

## IV. CONCLUSIONS

Using an empirical pseudopotential atomistic electronic structure theory,  $g$ -tensors of a large number of embedded InGaAs QDs with different shape, size, indium fraction and strain combinations are computed. This analysis provides the general traits of  $g$ -factor variation. For specific applications, when taken into account in their growth control or post-selection, it can be benefi-

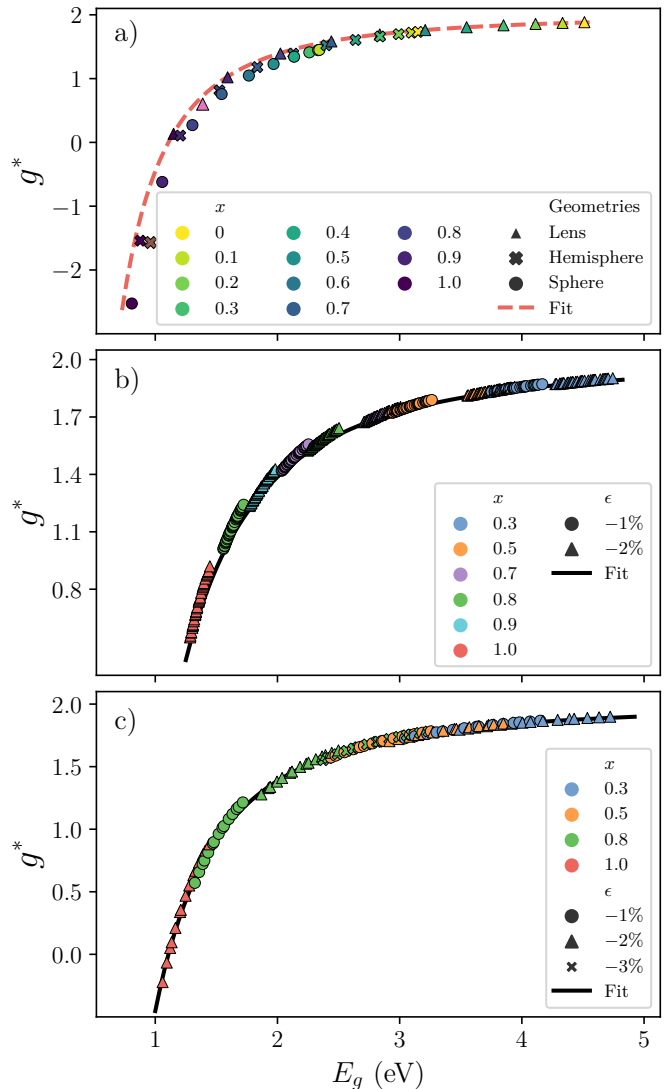


FIG. 5. Universal  $g$ -factor behavior obtained when the data for (a) different geometries in Fig. 2, (b)  $D$  series in Fig. 3, and (c)  $h$  series at  $D = 35$  nm in Fig. 4, are redrawn with respect to  $E_g$ . Two other literature data are shown in (a), as pink [31] and magenta [27] symbols. All fitted curves have the same equation,  $g^*(E_g) = 2 - (1.5665/E_g)^2$ .

cial for achieving  $g$ -near zero InGaAs QDs, or entitle ESR as a reliable tool for direct quantum logic operations. Our study also validates a recent report based on tight-binding electronic structure for compound QDs that the  $g$ -factor acquires a universal behavior with respect to the gap energy of the QD regardless of its structural details [47]. We additionally exhibit that this applies to alloy InGaAs QDs of various shapes and finite confinement allowing for penetration to the matrix. It remains to be examined whether these conclusions will be affected by an inhomogeneous atomic scale strain distribution within the QD.

## ACKNOWLEDGMENTS

We would like to thank TÜBİTAK, The Scientific and Technological Research Council of Turkey for financial support through the project No. 116F075. The numerical calculations reported in this paper were partially performed at TÜBİTAK ULAKBİM, High Performance and Grid Computing Center (TRUBA resources).

## APPENDIX: COMPUTATIONAL DETAILS

In this Appendix, we would like to give some further details about the computational implementation. We utilize our recently fitted empirical pseudopotentials for InAs and GaAs under various strain conditions to hybrid density functional theory band structures [63]. In anticipation to reduce matrix sizes, the fit was achieved with about 120 reciprocal lattice vectors within the energy cut-off. For the current work involving QDs having the  $\text{In}_x\text{Ga}_{1-x}\text{As}$  alloy core, we use the Vegard's law in mixing the compound InAs and GaAs pseudopotentials. As mentioned above the spin-orbit interaction over the  $p$ -states brings a further symmetric spin-orbit coupling parameter  $\lambda_S$  fitted to experimental spin-orbit splittings for bulk InAs and GaAs [63].

In the studied QDs, we exert strain to both matrix and the core material such that the same lattice constant uniformly applies over the full supercell. This greatly simplifies the computational tasks like the choice of the

basis sets, and allows the use of the standard fast Fourier transform in Eq. (3). For the latter, we utilize the FFTW library [64]. The non-self-consistent nature of the empirical pseudopotentials [58] necessitates an additional parameter to have a desirable band alignment under strain. Following Williamson *et al*, this is implemented as a hydrostatic strain-dependent pseudopotential formed as

$$V(q; \epsilon) = [1 + \gamma \epsilon_H] V(q), \quad (12)$$

where  $\gamma$  is the accompanying fitting parameter and  $\epsilon_H = \epsilon_{xx} + \epsilon_{yy} + \epsilon_{zz}$  refers to hydrostatic strain [60]. Within this scheme, we embed the QDs into an artificial matrix material of same FCC crystal structure that provides a conduction state core material confinement of about 300 meV, and much higher for the valence band up to about 3% uniform compressive strain.

The  $g$ -tensor expression in Eq. (11) requires, in principle, all of the QD states, but especially those energetically close to the state  $n$  under investigation. This demands well characterization of a large number of electronic states which hinges upon the strength of the LCBB basis set. We employ the bulk bands of the spinless top four (four) valence and the lowest four (one) conduction bands of the strained core (matrix) material. For either case, basis sets are formed from a three-dimensional  $5 \times 5 \times 5$  grid in the reciprocal space centered around the  $\Gamma$ -point. Its convergence is checked for the supercell size we adopted for calculations in this work. The final LCBB basis sets typically contain some two thousand elements.

- 
- [1] Y. Yafet,  $g$  factors and spin-lattice relaxation of conduction electrons, in *Solid state physics*, Vol. 14 (Elsevier, 1963) pp. 1–98.
  - [2] J. Callaway, *Quantum theory of the solid state* (Academic Press, 2013).
  - [3] M. A. T. Sandoval, J. E. Leon Padilla, A. Ferreira da Silva, E. A. de Andrada e Silva, and G. C. La Rocca, Mesoscopic  $g$ -factor renormalization for electrons in iii-v interacting nanolayers, *Phys. Rev. B* **98**, 075312 (2018).
  - [4] T. Nakaoka, S. Tarucha, and Y. Arakawa, Electrical tuning of the  $g$  factor of single self-assembled quantum dots, *Phys. Rev. B* **76**, 041301 (2007).
  - [5] Y. K. Kato and D. D. Awschalom, Electrical manipulation of spins in nonmagnetic semiconductors, *Journal of the Physical Society of Japan* **77**, 031006 (2008).
  - [6] F. Klotz, V. Jovanov, J. Kierig, E. C. Clark, D. Rudolph, D. Heiss, M. Bichler, G. Abstreiter, M. S. Brandt, and J. J. Finley, Observation of an electrically tunable exciton  $g$  factor in ingaas/gaas quantum dots, *Applied Physics Letters* **96**, 053113 (2010), <https://doi.org/10.1063/1.3309684>.
  - [7] J. Pingenot, C. E. Pryor, and M. E. Flatté, Electric-field manipulation of the landé  $g$  tensor of a hole in an  $\text{In}_{0.5}\text{Ga}_{0.5}\text{As}$ /gaas self-assembled quantum dot, *Phys. Rev. B* **84**, 195403 (2011).
  - [8] M. W. Taylor, P. Spencer, E. Clarke, E. Harbord, and R. Murray, Tuning exciton- $g$  factors in InAs/GaAs quantum dots, *J. Phys. D: Appl. Phys.* **46**, 505105 (2013).
  - [9] C. Santori, D. Fattal, J. Vučković, G. S. Solomon, and Y. Yamamoto, Indistinguishable photons from a single-photon device, *nature* **419**, 594 (2002).
  - [10] Y.-M. He, Y. He, Y.-J. Wei, D. Wu, M. Atatüre, C. Schneider, S. Höfling, M. Kamp, C.-Y. Lu, and J.-W. Pan, On-demand semiconductor single-photon source with near-unity indistinguishability, *Nature nanotechnology* **8**, 213 (2013).
  - [11] A. N. Vamivakas, Y. Zhao, C.-Y. Lu, and M. Atatüre, Spin-resolved quantum-dot resonance fluorescence, *Nature Phys.* **5**, 198 (2009).
  - [12] S. Yilmaz, P. Fallahi, and A. Imamoglu, Quantum-dot-spin single-photon interface, *Physical review letters* **105**, 033601 (2010).
  - [13] R. M. Stevenson, A. J. Hudson, A. J. Bennett, R. J. Young, C. A. Nicoll, D. A. Ritchie, and A. J. Shields, Evolution of entanglement between distinguishable light states, *Phys. Rev. Lett.* **101**, 170501 (2008).
  - [14] W. B. Gao, P. Fallahi, E. Togan, J. Miguel-Sánchez, and A. Imamoglu, Observation of entanglement between a quantum dot spin and a single photon, *Nature* **491**, 426 (2012).
  - [15] C. H. Schulte, J. Hansom, A. E. Jones, C. Matthiesen, C. Le Gall, and M. Atatüre, Quadrature squeezed pho-

- tons from a two-level system, *Nature* **525**, 222 (2015).
- [16] M. Kroner, K. M. Weiss, B. Biedermann, S. Seidl, S. Manus, A. W. Holleitner, A. Badolato, P. M. Petroff, B. D. Gerardot, R. J. Warburton, and K. Karrai, Optical detection of single-electron spin resonance in a quantum dot, *Phys. Rev. Lett.* **100**, 156803 (2008).
- [17] F. H. Koppens, C. Buizert, K.-J. Tielrooij, I. T. Vink, K. C. Nowack, T. Meunier, L. Kouwenhoven, and L. Vandersypen, Driven coherent oscillations of a single electron spin in a quantum dot, *Nature* **442**, 766 (2006).
- [18] B. Urbaszek, X. Marie, T. Amand, O. Krebs, P. Voisin, P. Maletinsky, A. Högele, and A. Imamoglu, Nuclear spin physics in quantum dots: An optical investigation, *Rev. Mod. Phys.* **85**, 79 (2013).
- [19] S. R. Hartmann and E. L. Hahn, Nuclear double resonance in the rotating frame, *Phys. Rev.* **128**, 2042 (1962).
- [20] P. London, J. Scheuer, J.-M. Cai, I. Schwarz, A. Retzker, M. B. Plenio, M. Katagiri, T. Teraji, S. Koizumi, J. Isoya, R. Fischer, L. P. McGuinness, B. Naydenov, and F. Jelezko, Detecting and polarizing nuclear spins with double resonance on a single electron spin, *Phys. Rev. Lett.* **111**, 067601 (2013).
- [21] G.-Q. Liu, Q.-Q. Jiang, Y.-C. Chang, D.-Q. Liu, W.-X. Li, C.-Z. Gu, H. C. Po, W.-X. Zhang, N. Zhao, and X.-Y. Pan, Protection of centre spin coherence by dynamic nuclear spin polarization in diamond, *Nanoscale* **6**, 10134 (2014).
- [22] S. R. Julian and M. R. Norman, Genetics and  $g$ -factors, *Nat. Physics* **7**, 191 (2011).
- [23] V. F. Mitrović, M. Horvatić, C. Berthier, S. A. Lyon, and M. Shayegan, Nmr study of large skyrmions in  $\text{al}_{0.13}\text{ga}_{0.87}\text{As}$  quantum wells, *Phys. Rev. B* **76**, 115335 (2007).
- [24] A. Ulhaq, Q. Duan, E. Zallo, F. Ding, O. G. Schmidt, A. I. Tartakovskii, M. S. Skolnick, and E. A. Chekhovich, Vanishing electron  $g$  factor and long-lived nuclear spin polarization in weakly strained nanohole-filled  $\text{gaas/algaas}$  quantum dots, *Phys. Rev. B* **93**, 165306 (2016).
- [25] M. Kuwahara, T. Kutsuwa, K. Ono, and H. Kosaka, Single charge detection of an electron created by a photon in a  $g$ -factor engineered quantum dot, *Appl. Phys. Lett.* **96**, 163107 (2010).
- [26] M. Bayer, A. Kuther, A. Forchel, A. Gorbunov, V. B. Timofeev, F. Schäfer, J. P. Reithmaier, T. L. Reinecke, and S. N. Walck, Electron and hole  $g$  factors and exchange interaction from studies of the exciton fine structure in  $\text{in}_{0.60}\text{ga}_{0.40}\text{As}$  quantum dots, *Phys. Rev. Lett.* **82**, 1748 (1999).
- [27] T. Nakaoka, T. Saito, J. Tatebayashi, and Y. Arakawa, Size, shape, and strain dependence of the  $g$  factor in self-assembled  $\text{in}(\text{ga})\text{as}$  quantum dots, *Phys. Rev. B* **70**, 235337 (2004).
- [28] T. Nakaoka, T. Saito, J. Tatebayashi, S. Hirose, T. Usuki, N. Yokoyama, and Y. Arakawa, Tuning of  $g$ -factor in self-assembled  $\text{in}(\text{ga})\text{as}$  quantum dots through strain engineering, *Phys. Rev. B* **71**, 205301 (2005).
- [29] T. P. M. Alegre, F. G. G. Hernández, A. L. C. Pereira, and G. Medeiros-Ribeiro, Landé  $g$  tensor in semiconductor nanostructures, *Phys. Rev. Lett.* **97**, 236402 (2006).
- [30] Exciton fine structure in  $\text{ingaas}$ , .
- [31] A. Schwan, B.-M. Meiners, A. B. Henriques, A. D. B. Maia, A. A. Quivy, S. Spatzek, S. Varwig, D. R. Yakovlev, and M. Bayer, Dispersion of electron  $g$ -factor with optical transition energy in  $\text{(in,ga)as/gaas}$  self-assembled quantum dots, *Applied Physics Letters* **98**, 233102 (2011), <https://doi.org/10.1063/1.3588413>.
- [32] A. Schwan, B.-M. Meiners, A. Greulich, D. R. Yakovlev, M. Bayer, A. D. B. Maia, A. A. Quivy, and A. B. Henriques, Anisotropy of electron and hole  $g$ -factors in  $\text{(in,ga)as}$  quantum dots, *Applied Physics Letters* **99**, 221914 (2011), <https://doi.org/10.1063/1.3665634>.
- [33] L. Sapienza, R. Al-Khuzheyri, A. Dada, A. Griffiths, E. Clarke, and B. D. Gerardot, Magneto-optical spectroscopy of single charge-tunable  $\text{inas/gaas}$  quantum dots emitting at telecom wavelengths, *Phys. Rev. B* **93**, 155301 (2016).
- [34] H. M. G. A. Tholen, J. S. Wildmann, A. Rastelli, R. Trotta, C. E. Pryor, E. Zallo, O. G. Schmidt, P. M. Koenraad, and A. Y. Silov, Strain-induced  $g$ -factor tuning in single  $\text{ingaas/gaas}$  quantum dots, *Phys. Rev. B* **94**, 245301 (2016).
- [35] H. M. G. A. Tholen, J. S. Wildmann, A. Rastelli, R. Trotta, C. E. Pryor, E. Zallo, O. G. Schmidt, P. M. Koenraad, and A. Y. Silov, Active tuning of the  $g$ -tensor in  $\text{ingaas/gaas}$  quantum dots via strain, *Phys. Rev. B* **99**, 195305 (2019).
- [36] S. Wu, K. Peng, X. Xie, J. Yang, S. Xiao, F. Song, J. Dang, S. Sun, L. Yang, Y. Wang, S. Shi, J. He, Z. Zuo, and X. Xu, Electron and hole  $g$  tensors of neutral and charged excitons in single quantum dots by high-resolution photocurrent spectroscopy, *Phys. Rev. Applied* **14**, 014049 (2020).
- [37] A. A. Kiselev, E. L. Ivchenko, and U. Rössler, Electron  $g$  factor in one- and zero-dimensional semiconductor nanostructures, *Phys. Rev. B* **58**, 16353 (1998).
- [38] C. E. Pryor and M. E. Flatté, Landé  $g$  factors and orbital momentum quenching in semiconductor quantum dots, *Phys. Rev. Lett.* **96**, 026804 (2006).
- [39] R. Zielke, F. Maier, and D. Loss, Anisotropic  $g$  factor in  $\text{inas}$  self-assembled quantum dots, *Phys. Rev. B* **89**, 115438 (2014).
- [40] K. Gawarecki, Spin-orbit coupling and magnetic-field dependence of carrier states in a self-assembled quantum dot, *Phys. Rev. B* **97**, 235408 (2018).
- [41] A. Mielnik-Pyszcorski, K. Gawarecki, and P. Machnikowski, Limited accuracy of conduction band effective mass equations for semiconductor quantum dots, *Scientific reports* **8**, 1 (2018).
- [42] C. J. Delerue and M. Lannoo, *Nanostructures: theory and modeling* (Springer Science & Business Media, 2013).
- [43] M. Usman, Atomistic theoretical study of electronic and polarization properties of single and vertically stacked elliptical  $\text{inas}$  quantum dots, *Phys. Rev. B* **86**, 155444 (2012).
- [44] C. E. Pryor and M.-E. Pistol, Atomistic k.p theory, *Journal of Applied Physics* **118**, 225702 (2015).
- [45] A. Mittelstädt, L. A. T. Greif, S. T. Jagsch, and A. Schliwa, Efficient electronic structure calculations for extended systems of coupled quantum dots using a linear combination of quantum dot orbitals method, *arXiv preprint arXiv:1912.03983* (2019).
- [46] L. M. Roth, B. Lax, and S. Zwerdling, Theory of optical magneto-absorption effects in semiconductors, *Phys. Rev.* **114**, 90 (1959).
- [47] A. Tadjine, Y.-M. Niquet, and C. Delerue, Universal behavior of electron  $g$ -factors in semiconductor nanostructures, *Phys. Rev. B* **95**, 235437 (2017).

- [48] F. Guffarth, R. Heitz, A. Schliwa, O. Stier, N. N. Ledentsov, A. R. Kovsh, V. M. Ustinov, and D. Bimberg, Strain engineering of self-organized inas quantum dots, *Phys. Rev. B* **64**, 085305 (2001).
- [49] M. Usman, V. Tasco, M. T. Todaro, M. De Giorgi, E. P. O'Reilly, G. Klimeck, and A. Passaseo, The polarization response in inas quantum dots: theoretical correlation between composition and electronic properties, *Nanotechnology* **23**, 165202 (2012).
- [50] C. Bulutay, Quadrupolar spectra of nuclear spins in strained  $\text{In}_x\text{Ga}_{1-x}\text{As}$  quantum dots, *Phys. Rev. B* **85**, 115313 (2012).
- [51] L.-W. Wang and A. Zunger, Linear combination of bulk bands method for large-scale electronic structure calculations on strained nanostructures, *Phys. Rev. B* **59**, 15806 (1999).
- [52] C. Bulutay, Interband, intraband, and excited-state direct photon absorption of silicon and germanium nanocrystals embedded in a wide band-gap lattice, *Phys. Rev. B* **76**, 205321 (2007).
- [53] H. Yildirim and C. Bulutay, Bound-state third-order optical nonlinearities of germanium nanocrystals embedded in a silica host matrix, *Phys. Rev. B* **78**, 115307 (2008).
- [54] C. Bulutay, M. Kulakci, and R. Turan, Stark effect, polarizability, and electroabsorption in silicon nanocrystals, *Phys. Rev. B* **81**, 125333 (2010).
- [55] D. Gunceler and C. Bulutay, dc-switchable and single-nanocrystal-addressable coherent population transfer, *Applied Physics Letters* **97**, 241909 (2010), <https://doi.org/10.1063/1.3526751>.
- [56] Ü. Keleş, B. Liedke, K.-H. Heinig, and C. Bulutay, Networks of silicon nanowires: A large-scale atomistic electronic structure analysis, *Applied Physics Letters* **103**, 203103 (2013), <https://doi.org/10.1063/1.4830039>.
- [57] Ü. Keleş, A. Çakan, and C. Bulutay, Disorder-free localization around the conduction band edge of crossing and kinked silicon nanowires, *Journal of Applied Physics* **117**, 064308 (2015), <https://doi.org/10.1063/1.4907585>.
- [58] G. Bester, Electronic excitations in nanostructures: an empirical pseudopotential based approach, *J. Phys.: Condens. Matter* **21**, 023202 (2008).
- [59] M. S. Hybertsen and S. G. Louie, Spin-orbit splitting in semiconductors and insulators from the ab initio pseudopotential, *Phys. Rev. B* **34**, 2920 (1986).
- [60] A. J. Williamson, L. W. Wang, and A. Zunger, Theoretical interpretation of the experimental electronic structure of lens-shaped self-assembled inas/gaas quantum dots, *Phys. Rev. B* **62**, 12963 (2000).
- [61] L. M. Roth,  $g$  factor and donor spin-lattice relaxation for electrons in germanium and silicon, *Phys. Rev.* **118**, 1534 (1960).
- [62] G. Medeiros-Ribeiro, E. Ribeiro, and H. Westfahl Jr,  $g$ -factor engineering and control in self-assembled quantum dots, *Appl. Phys. A* **77**, 725 (2003).
- [63] A. Çakan, C. Sevik, and C. Bulutay, Strained band edge characteristics from hybrid density functional theory and empirical pseudopotentials: GaAs, GaSb, InAs and InSb, *J. Phys. D: Appl. Phys.* **49**, 085104 (2016).
- [64] M. Frigo, A fast fourier transform compiler, in *Proceedings of the ACM SIGPLAN 1999 conference on Programming language design and implementation* (1999) pp. 169–180.